

January 5, 2021

# The dynamics of quasi-periodic ripples in the high-latitude F-region.

M. J. Birch<sup>1</sup>

J.K. Hargreaves<sup>1,2</sup>

(1) Jeremiah Horrocks Institute for Mathematics, Physics and Astronomy,  
University of Central Lancashire, Preston, UK.

(2) Department of Physics, Lancaster University, UK.

## **Abstract**

This study extends the investigation of quasi-periodic ripples in the F-region electron content reported by Birch and Hargreaves (2020a) to determine their flow velocity and wavelength, using data from the EISCAT Svalbard radars (the 42m antenna being field-aligned and the 32m scanning in a circular pattern at a fixed angle from the field). The ripples were extracted from the 42m electron content between altitudes 213 and 389 km in the noon and midnight sectors using a bandpass filter which reduces the noise component while removing long-term trends. These ripples were found to have an average periodicity of about 21 minutes in the noon sector and 27 minutes at night. Using the 32m line-of-sight velocity data,

they were also found to propagate in the noon sector at about 467 m/s in a westerly direction with a wavelength of 581 km, and in the night sector at about 283 m/s in a southerly direction with a wavelength of 454 km. The directions compare favourably with modelled plasma flows from the SuperDARN network of coherent scatter radars.

## 1 Introduction

In a previous study, Birch and Hargreaves (2020a) (subsequently cited as B&H) reported the existence of persistent quasi-periodic ripples in the F-region electron content, and traced their likely origin, first to the geomagnetic field, and thence to the IMF and the solar wind at L1. This study extends the investigation of these F-region ripples with the objective of determining their speed, direction, and wavelength.

Using the 42m field-aligned antenna, the frequency of the ripples is determined by integrating the electron density between 213 and 389 km to give the electron content. The ripples are then revealed using a band-pass filter based on a ratio of running means, from which the frequency is determined. The 32m antenna, operating in a circular scan pattern, provides the line-of-sight velocity data, the horizontal component of which is used to extract the plasma flow speed and direction during intervals when a steady stream is present. From the frequency and speed of the ripples, the wavelength can be readily determined. However, even with the velocity observations, it is not possible to determine with certainty the nature of the ripples i.e. whether they are waves or convecting density structures.

The ripples in the F-region electron content were first reported by Hargreaves and Birch (2018), and then in more detail by B&H. From data selected over many different years and spacecraft from 1978 to 2016, ripples of similar frequency were later revealed in the solar wind and the IMF from 1 to 40 AU, and in the planetary magnetospheres of Earth, Jupiter and Saturn (Birch and Hargreaves, 2020b). This phenomenon therefore appears to be persistent throughout the solar system, and it is suggested in Birch and Hargreaves (2020a, 2020b) that these ripples might originate from pressure and gravity waves present in the Sun.

## 2 Observations

On August 22-23 2019 observations were made with the EISCAT Svalbard 32m and 42m radars at Longyearbyen (78.153°N, 16.029°E, L-value 14.9): from 22/0900 to 22/1300 UT, and from 22/2100 to 23/0100 UT, covering four hours in each of the noon and midnight sectors. For operational reasons there was a gap of 1 hour in the noon observations (from 1020 to 1120 UT), so the noon sector run was repeated on October 1 (from 0906 to 1242 UT). A summary of these times is given in Table 1.

Date	UT	LT	Duration (hours)	Sector
August 22	09:00 - 10:20	10:04 - 11:24	3.0	noon
	11:21 - 13:00	12:25 - 14:04		
August 22-23	21:00 - 01:00	22:04 - 02:04	4.0	midnight
October 1	09:06 - 12:42	10:10 - 13:46	3.6	noon

Table 1: Concurrent observing periods with the 32m and 42m EISCAT Svalbard radars.

The 42m antenna is field-aligned (azimuth  $-175.5^\circ$ , elevation  $81.6^\circ$ ), whereas the 32m antenna was driven in a circular scan pattern at two fixed angles ( $30^\circ$  and  $45^\circ$ ) from the field (Figure 1). The duration of each  $360^\circ$  rotation was 9m36s, giving a scan rate of about  $0.6^\circ/\text{s}$ . The two scans were alternated, the  $30^\circ$  being anti-clockwise and the  $45^\circ$  being clockwise, with the transition between each scan occurring in the south. The antenna elevation varied continuously throughout each scan, the geometry having been designed to maintain a fixed angle from the field. In addition to electron density, the radar observations also included line-of-sight velocity, and the antenna pointing angles (azimuth and elevation). (The electron and ion temperature, also available, were not used in this study.)

All the data are at 32s resolution, except the 42m in August which are at 64s resolution. For the 32m scans, this gives about 18 datapoints per rotation, or 1 every  $20^\circ$ . The F-region height range of interest was from 213 to 389 km, and the half-power beam-width was  $\pm 0.3^\circ$ .

## 3 Frequency of the ripples in electron content and density from the 42m observations

### 3.1 Electron content ratios

The 42m electron density variations during the October noon period are shown in Figure 2 (the August noon and midnight periods are similar in appearance). Using the same method as B&H, the electron content along the radar beam over the height range 213 to 389 km was derived by integrating the electron density in slabs centred on heights at 228, 245, 262, 281, 300, 320, 342 and 365 km, giving a mean slab thickness of about 20 km.

To reduce the noise component, and to remove long-term trends, a bandpass filter was used in which the 42m electron content data were averaged over 6 minutes and this value was then divided by the average over 30 minutes, giving the electron content variations as a *ratio*. (In Birch and Hargreaves (2020b) the method is validated by comparisons with finite impulse response filtering, Fourier and wavelet analyses, and auto-correlation tests on natural (non-pseudo-) random data from radioactive decay.)

Figure 3 shows the variations in the electron content ratio during the three observing periods in Table 1 (the  $3\sigma$  errors, which are clearly insignificant for our purposes, are denoted by the dotted lines). (For continuity, in this and subsequent figures involving time series, 00:00 to 01:00 UT on August 23 is shown as 24:00-25:00 UT.) As in B&H, the variations appear to be quasi-periodic in nature, at most times consisting of a series of distinct peaks and dips. The 21 inter-peak periods (IPPs) between the 25 selected peaks over a total of 10.6 hours are summarised as a histogram (Figure 4). In this study, a magnitude limit was not imposed on peak selection because only one instance (at 11:30 on August 22) is less than magnitude 1.03 (the limit adopted in B&H), and this is a distinct example.

### 3.2 Electron density ratios at selected heights

The integration of electron density (over the height range 213 to 389 km) to give electron content was justified in B&H because the correlation coefficient between the electron density time series at adjacent pairs of heights about 20 km apart was only once less than 0.9, and for a vertical separation of 154 km it was still 0.86. However, when the same test is conducted for the 42m electron density time series in this study, the correlation coefficient between different heights is not as convincing. For example, Figure 5a shows the correlations for the August noon sector (those for the midnight sector on August 22-23 and the noon sector on October 1 gave a similar response). However, when the time series are smoothed to 6-minutes (Figure 5b) the correlations improve considerably, but when smoothed to 12-minutes (Figure 5c) there is little further improvement (implying that the poor response in (a) might be due to noise). Nevertheless, the correlations in (b) are not as significant as in B&H. Consequently, as an alternative to electron content, the IPP analysis in Section 3.1 was repeated for electron density ratios, at heights 213, 300 and 389 km.

For example, the electron density ratios at 300 km for the three periods in Table 1, derived using the same smoothing procedure as the electron content ratios, are shown in Figure 6 (the  $3\sigma$  errors are denoted by the dotted lines). The same quasi-periodic ripples are present, though the structures are more erratic at times, which might be expected, given that these data are not integrated over a range of heights. The same procedure was applied to heights 213 and 389 km, and the IPPs were measured over a total of 10.6 hours for all 3 heights. The results are summarised in Figure 7, and it is apparent that the median IPP is about the same at each height, varying between 18 and 20 minutes. The lower quartile is also fairly constant (14 to 15 minutes), whereas the upper quartile (and therefore the inter-quartile range) decreases progressively with increasing height, from 29 minutes (213 km) to 20 minutes (389 km).

The statistics are summarised in Table 2, and clearly there is good agreement between the IPPs derived from the electron content ratios and those from the electron density ratios

at the three selected heights. In the subsequent analysis, 300 km (about the middle of the height range) will be used as the representative height when considering electron density ratios.

Ratio (6/30)	Height (km)	Inter-peak period (mins)				Samples
		LQ	MD	UQ	IQ	
EC	213 - 389	17	20	28	9	21
Ne	389	14	18	20	6	28
	300	14	19	25	11	24
	213	15	20	29	14	20

Table 2: Summary of inter-peak period statistics for electron density and electron content ratios for all 3 observing periods combined, a total of 10.6 hours. (Key: EC electron content; Ne electron density; LQ lower quartile; MD median; UQ upper quartile; IQ inter-quartile range.)

## 4 Velocity of the plasma flow from the 32m observations

In the above analysis it has been shown that, on average, the IPP of the ripples is about 20 minutes (using electron content), and about 19 minutes (using electron density at 300 km). Over shorter time intervals this value will vary, but should usually be within the quartiles (Table 2). A question now arises: are there intervals during the observations when the flow speed and direction of the plasma can be determined from the line-of-sight velocity data? Attention will focus on the 32m velocities and azimuth angles in an attempt to answer this question, in Section 4.2 using the median velocity over all heights (which relates to the electron content ratio), and in Section 4.3 using the velocity at 300 km (which relates to the electron density ratio at that height).

The line-of-sight velocity (measured along the 32m beam) is a component of the actual velocity (which is assumed to be horizontal), the conversion factor being  $1/\cos(\text{elevation})$ . As the 32m antenna rotates through each  $360^\circ$  sweep, in the presence of a steady plasma

flow the line-of-sight velocity varies between zero (when the flow is orthogonal to the beam) and maxima (when the flow is towards or away from the antenna, parallel to the beam).

Unlike the electron content (which usually comprises a lower intensity fluctuation superimposed on a higher intensity background), the velocities oscillate both positively and negatively (away from and towards the 32m antenna as it rotates) with a median speed that is negligible in the long term. For example, over the observing periods, the median values are: August (noon) 26 m/s; August (midnight) 24 m/s; October (noon) 16 m/s. Furthermore, because of the rate at which the antenna scans (about  $38^\circ/\text{min}$ ), the use of a 6-minute running mean (and, consequently, 6min/30min bandpass filtering) is not feasible for the velocity data.

The 32s time series of the median horizontal velocity, over all 10 heights, for the three observing periods, together with the scan azimuth, are shown in Figure 8. (The  $3\sigma$  errors, which are clearly insignificant for our purposes, are denoted by the black dotted lines, and the azimuths are in blue). Though there is considerable variability, inspection of the plots reveals that the velocity structures in some intervals appear to be periodically synchronised with the azimuth.

#### 4.1 Estimation of the velocity during selected intervals

With the aim of quantifying the time dependency of velocity relative to azimuth, and thus assisting in the selection of intervals when a steady flow is present, Figure 9 shows the velocity when the scan azimuth is within  $10^\circ$  of N/S and E/W (with positive speed for N and E, negative for S and W). As the scanner rotates, observations are taken about every  $20^\circ$ , so each of the four orthogonal  $20^\circ$  sectors usually contains a single data-point. However, there are occasionally groups of 2 or 3 in the S sector because this is the direction in which the elevation changes between each scan, and in these cases the solid line denotes the mean values.

Though the variability noted in Figure 8 is still present, during the August noon period

(Figure 9a) the E/W plot shows evidence of a strong, well-defined westerly flow in the interval 11:21-13:00 UT (median speed 450 m/s), with a weak, less consistent westerly flow in the interval 09:00-10:20 UT, (the N/S plot shows no clear distinction, as would be expected from a W flow). During the August night period (Figure 9b), the N/S plot shows that, with the exception of one data-point to the N, a consistent southerly flow is present in the interval 21:00-22:18 UT (median speed 212 m/s), but there is no clear distinction in the interval 22:18-25:00 UT. (For the E/W plot the opposite is the case, as expected: there is no clear distinction in the interval 21:00-22:18 UT, but from 22:18 to 25:00 (August 23 at 01:00) UT a less consistent but predominantly westerly flow is evident.) Finally, during the October noon period (Figure 9c), the E/W plot shows that, with the exception of 3 data-points in the E, a predominantly W flow is present at all times (median speed 421 m/s).

These estimates of the speed and direction of the plasma flow during the three selected intervals are summarised in Table 3. An attempt will next be made to improve these estimates by plotting velocity against azimuth for the three intervals.

Interval			Speed (m/s)	Direction
Date	UT	LT		
August 22	11:21-13:00	12:28-14:04	450	W
	21:00-22:18	22:04-23:22	212	S
October 1	09:06-12:42	10:10-13:46	421	W

Table 3: Estimate of the flow speed and direction for the intervals selected from Figure 9

(The velocity analysis used in Sections 4.2 and 4.3 is based on 32s data smoothed to 64 seconds, which was found to suppress noise while leaving the significant structures intact. This analysis was repeated using the 32s data and, though there is greater variability, the difference between the resulting flow speeds and directions was found to be negligible.)

## 4.2 Determination of the median velocity over all heights during the selected intervals

It has been demonstrated that in the August and October noon sectors there is an implied westerly flow (zero speed in the north and south, with maximum speed in the east-west direction, away from the antenna in the west, and towards it in the east). In the August midnight sector the flow dynamics are much less distinct than in the two noon sectors, but nonetheless there is evidence of a weaker southerly flow.

The median velocity during the selected intervals in Table 3 can be more precisely determined by plotting velocity against azimuth (smoothed to 64 seconds), as in Figure 10, in which the  $30^\circ$  and  $45^\circ$  sweeps are merged as a total population (this is possible because both sweeps have been normalised to the horizontal). The solid lines represent the median for all sweeps combined, the dashed lines indicate the quartiles (the reliability of which is discussed below), and the dotted lines connect each  $360^\circ$  sweep of the antenna. (The data-points are aligned by azimuth in Figure 10c because, for reasons unknown, in the October observations the azimuths repeated almost exactly for each sweep of the antenna, whereas in the August observations this was not the case.)

Using the median line for each selected interval, the speed of the flow is quantified by taking the mean of the absolute values of the velocities at the maxima, both positive and negative, when the flow is along the beam. The azimuths at the maxima also indicate the direction of flow: at a positive maximum the flow is away from the antenna, and at a negative maximum the flow is towards it. In addition, when the median line crosses the abscissa, the flow is orthogonal to the azimuth of the beam (this occurs at a maximum of three points). Thus five azimuths (at most) can be deduced from the plots, the mean of which gives an estimate of the direction of the flow (in some cases an azimuth was uncertain, but at least four were valid in each of the three intervals).

For example, in Figure 10a the speed is  $(|450| + |-425|)/2 = 438$  m/s. At the peak the azimuth is  $-80^\circ$ (away), and at the dip it is  $+80^\circ$ (towards) =  $-100^\circ$ (away), together

indicating that the flow is in about a westerly direction. In the vicinity of  $-180^\circ$  the median does not cross the zero velocity axis so the azimuth is uncertain. However, at the other two zero velocity crossings the azimuth is  $+10^\circ$  and  $+175^\circ$ , but the flow is orthogonal, giving  $-80^\circ$  and  $-95^\circ$ . The flow direction is therefore the mean of  $[-80, -100, -80, -95]$ , giving  $-89^\circ$ , or almost due W. Using this technique, the flow speeds and directions in Table 4a were estimated from the median velocities in Figure 10, and the results are not dissimilar to those in Table 3.

In these velocity-azimuth plots, when calculating the median and quartiles, an azimuth interval of  $20^\circ$  was chosen as a compromise between the provision of (1) sufficient samples for determining the median at each point on the curve and (2) a curve with sufficient continuity for a speed and direction to be deduced. In the October population the sample sizes in the  $20^\circ$  azimuth intervals range from 20 to 34, whereas in the two August populations they range from 6 to 14. However, this difference is balanced by the fact that the spread of data-points in October is considerably greater than that in August. Nonetheless, the quartiles should be treated with some caution, particularly those for August. (Of course, the longer the observing period, the more scans and hence the more data-points are available, but the less likely will it be that the F-region drift velocity will remain constant.)

### **4.3 Determination of the velocity at 300 km during the selected intervals**

As well as the median velocity over the full height range, the variation with azimuth of the velocity at height 300 km was also investigated. It was found that this gives a similar response to Figure 10, except that there is greater variability because these velocities are not median values over all 10 heights. The speed and direction of the plasma flow were deduced using the same procedure described in Section 4.2. The results are shown in Table 4b, in which it is clear that the flow speeds and directions derived using the velocity at height 300 km are very similar similar to those derived using the median velocity over all heights (Table

Interval			Sector	Peak samples	42m IPP (T mins)	Speed (v)		Direction (degrees)	Wavelength (v.T km)
Date	UT	LT				m/s	km/min		
(a) from electron content ratios and velocities between 213 and 389 km.									
August 22	11:24-13:00	12:28-14:04	noon	5	22	438	26.3	-89 (W)	579
	21:00-22:18	22:04-23:22	night	3	27	280	16.8	-179 (S)	454
October 1	09:06-12:42	10:10-13:46	noon	11	20	485	29.1	-81(WxN)	582
(b) from electron density ratios and velocities at 300 km.									
August 22	11:24-13:00	12:28-14:04	noon	5	19	415	24.9	-85 (W)	473
	21:00-22:18	22:04-23:22	night	3	26	270	16.2	-186 (S)	421
October 1	09:06-12:42	10:10-13:46	noon	12	16	485	29.1	-82 (WxN)	466

Table 4: Summary of ripple dynamics for the three selected intervals (IPP = inter-peak period). Uncertainty estimates are not included because the selected time intervals provide insufficient samples for the determination of representative values.

4a). (It is considered, however, that the results derived from the median velocity over the full height range are more representative of the actual flow dynamics than those derived from the velocity at a single height.)

#### 4.4 Estimated flow directions from SuperDARN

The SuperDARN system of coherent scatter radars (Greenwald et al., 1995) provides F-region circulation maps, and those for the middle of our three selected intervals are shown in Figure 11. The direction of flow in the negative (blue) cell is clockwise, and that in the positive (red) cell is anti-clockwise, parallel to the cell contours. However, during the periods in question there were no SuperDARN observations in the vicinity of Longyearbyen (indicated by an "L" in the figure), so the circulation cell contours at this location are based on modelled data under the prevalent solar wind conditions. Nonetheless, the circulation contours provide a general indication of the flow direction and are worthy of consideration.

In Figure 11(a,c) the cell contours in both noon sectors imply a flow at Longyearbyen which is slightly north of west (the contours in (c) being more clearly defined than those in (a)). In Figure 11b (21:38 UT) Longyearbyen appears to be approaching the point in the night sector where the direction of flow implied by the cell geometry is in transition from south to east. However, equivalent maps at 21:18 and 22:00 UT show that the ESR experiences a persistent southerly flow throughout the 21:00-22:18 UT interval.

The flow directions in Table 4 are indicated by the black arrows in the maps, and it is evident that, in general, they agree with the directions implied by the cell contours summarised above.

## 5 Ripple wavelengths in the three selected intervals

From the measurements in Section 3, the average IPP was determined for the electron content and electron density ripples during each of the three intervals in Tables 3 and 4, in which the number of peaks is no more than 12 and as few as 3. These sample sizes are smaller than those used for the combined results in Table 2 (in which the averages are medians) and there are no extreme values; consequently, the mean IPP was considered to be more representative. The values are shown in column 6 of Table 4 (16 to 27 mins), and they are not dissimilar to the overall results in Table 2 (18 to 20 mins).

In Section 4, the speed and direction of the plasma flow during the three selected intervals were estimated (Table 3), and then more accurate results were determined (Table 4). In Table 4, from the inter-peak period of the ripples ( $T$  mins, column 6), and the speed of the plasma flow ( $v$  km/min, column 8), the wavelength of the ripples can be estimated ( $\lambda = v.T$  km, column 10). (It is assumed that the electron density and line-of-sight velocity can be related because both quantities are derived from measurements of the same electron population.) However, whether these ripples are actually waves (with a wavelength and a frequency) or convecting density structures (with an inter-structure spatial distance and a periodicity) remains uncertain, and is discussed below. It is clear from Table 4 that the

wavelengths derived from the electron content are not dissimilar to those derived from the electron density at 300 km, the differences being mainly due to the 42m IPP.

Uncertainty estimates are not included in Table 4 because the selected time intervals provide an insufficient number of ripples for the determination of representative statistics.

## 6 Discussion

Observations of electron density on February 27-28 and March 1-2 2015 with the 42m EISCAT Svalbard radar (ESR), covering 24 hours of observations, revealed evidence of electron content structures in the high-latitude F-region between 237 and 355 km having average period 22 minutes (Hargreaves and Birch, 2018). Similar ripples with an average periodicity of 25 minutes were also reported in B&H from observations covering a total of 158 hours over 10 days in three different seasons during 2012, 2015 and 2017. The F-region ripples identified in the current study also have a similar periodicity (27 minutes in the night sector, and an average of 21 minutes in the two noon sectors). Our studies therefore suggest that this phenomenon is a persistent and widespread characteristic of the F-region.

The convection in the high-latitude ionosphere is the result of two intrinsically time-dependent mechanisms (Lockwood et al., 1990), one driven by solar wind-magnetosphere coupling at the dayside magnetopause, the other by the release of energy in the geomagnetic tail (mainly by dayside and nightside reconnection, respectively). The resulting circulation pattern is a twin-cell structure (Zhang et al., 2007), the dusk-side cell rotating in a clockwise direction and the dawn-side cell in an anti-clockwise direction. The ripples identified herein appear to be a persistent feature of this twin-cell structure.

In B&H, the likely origin of the ripples in the F-region was traced to the geomagnetic field, and thence to the IMF and the solar wind at L1. The prevalence of ionospheric fluctuations of a similar frequency as those identified herein is supported by related studies based on locations covering a wide range of geographic locations and L-values (Table 5, including the current study for comparison). Prikryl et al. (2005) report that HF radar ground-scatter

signatures of travelling ionospheric disturbances (TIDs) caused by atmospheric gravity waves with periods from 20 to 40 minutes have been traced to pulsed ionospheric flows (PIFs) at high latitudes. These, in turn, result from bursts in the convection electric field and/or the associated ionospheric current fluctuations inferred from ground magnetic field perturbations. PIFs and TIDs are significant in the context of solar-terrestrial interaction because they correlate with Alfvénic fluctuations of the interplanetary magnetic field observed in high speed solar wind streams. This correlation indicates a very direct coupling of energy from the solar wind to the sub-auroral atmosphere.

Incoherent scatter radar (ISR) observations at Arecibo, Millstone Hill, and Poker Flat made by Livneh et al. (2009) have revealed the presence of coherent omnipresent fluctuations in the ionosphere (COFIs) with periods ranging from about 30 to 60 minutes, with vertical wavelengths increasing with altitude from tens to hundreds of kilometres. High-pass filtering of the ISR data reveals that the COFIs are persistently seen in Arecibo results from 22-23 March 2004, 5-6 June, 21-25 September 2005, and 17-20 November 2005, and Millstone Hill results from 4 October to 4 November 2002. The COFIs are strong throughout the F-region, often spanning altitudes from 160 km to above 500 km, and are detected during both day and night in the F2 layer at all times and altitudes when there is sufficient plasma to generate them.

In a multi-station analysis of geomagnetic field measurements, Villante et al. (2010) report that persistent simultaneous oscillations at discrete frequencies (including  $\approx 1.0$  mHz, or 17 minutes periodicity) are detected, from low to high latitudes, at all local times. It was found that they are driven by fluctuations of the solar wind dynamic pressure at the same frequencies, via the modulation of the magnetopause current, and that several aspects of the geomagnetic field observations show a clear latitudinal and local time dependence.

Guo et al. (2016) studied a long-duration outward propagating Alfvén wave carried by a high-speed solar wind stream which produced electron density disturbances in the Earth's thermosphere by exciting multiple large-scale gravity waves in auroral regions. The

disturbances were observed continuously over  $\approx 2$  days, with amplitudes of up to  $\pm 40\%$  of background. It is concluded that the observed ability of Alfvén waves to excite large-scale gravity waves, and the fact that they are continuously present in both the solar atmosphere and the solar wind, suggest that Alfvén waves could be an important solar-interplanetary driver of global thermospheric disturbances.

Over a period of about 7 days, Guo et al. (2019) observed sequential large-scale gravity waves propagating from northern and southern auroral regions that are clearly linked to intermittent Alfvénic fluctuations in the southward magnetic fields embedded in three successive solar wind stream interaction regions. It is suggested that Alfvénic fluctuations might play a role in the solar wind-magnetosphere interaction, leading to impulsive auroral electrojet activity which in turn excites sequential gravity waves.

The above citations provide supporting evidence for the existence of widespread, persistent quasi-periodic ripples in the F-region over a broad range of magnetic latitudes and local times.

There is also evidence for structures with similar periodicity in the D-region. For example, observations of VLF radio signals at 24 kHz emitted by the communications transmitter in Maine, USA (station ID: NAA;  $44.6^\circ\text{N}$ ,  $67.2^\circ\text{W}$ ) were made by Hayes et al. (2017) using the Stanford University Sudden Ionospheric Disturbance monitor at the Rosse Solar-Terrestrial Observatory in Birr, Ireland ( $53.1^\circ\text{N}$ ,  $7.9^\circ\text{W}$ ). D-region fluctuations of period  $\approx 20$  minutes are reported, which were synchronised with a set of pulsating solar flare loops. The differential VLF and X-ray flare amplitudes give a correlation coefficient of 0.94.

Observations by Hargreaves and Birch (2018) of the electron density on February 27-28 and March 1-2 2015 with the 42m EISCAT Svalbard radar revealed evidence of a D-region absorption layer peaking at 80-85 km. This deduced absorption was found to exhibit a quasi-periodic variation of about 23 minutes, remarkably similar to the electron content structures in the F-region reported in the same study.

Station or group name, and location	Year of observations	Geographic Position	L-value	IPP (mins)	Citation
EISCAT Svalbard radar (32m and 42m)	2019	78.15° N 16.03° E	14.9	21	This study
EISCAT Svalbard radar (42m)	2012, 2015, 2017	78.15° N 16.03° E	14.5, 14.7, 14.8	25	Hargreaves and Birch (2020a)
EISCAT Svalbard radar (42m)	2015	78.15° N 16.03° E	14.7	22	Hargreaves and Birch (2018)
EISCAT VHF radar, Tromsø	2008	69.59° N 19.23° E	6.0	20	Birch et al. (2013)
IRIS imaging riometer, Kilpisjärvi		69.05° N, 20.79° E	5.9		
Hankasalmi SuperDARN radar, Finland	1999	62.32° N 26.61° E	3.8	20 to 40	Prikrýl et al. (2005)
Ny Alesund magnetometer, Svalbard		78.92° N 11.91° E	16.3		
Longyearbyen magnetometer, Svalbard		78.15° N 16.03° E	14.0		
Arecibo ISR, Puerto Rico	2004, 2005	18.35° N 66.75° W	1.3	30 to 60	Livneh et al. (2009)
Millstone Hill ISR, Westford, USA	2002	42.61° N 71.49° W	2.7		
European magnetometer chain (12 stations)	1998	37.5° E (average)	1.5 to 6.7	17	Villante et al. (2010)
N. American magnetometer chain (9 stations)		120° W (average)	1.7 to 20.4		
VLF transmitter, Cutler, Maine, USA	2016	44.64° N 67.28° W	2.9	20	Hayes et al. (2017)
Roske Observatory, Birr, Ireland		53.10° N 7.91° W	3.2		

Table 5: Name, location, year of observations, geographic position, and L-value of all stations cited in the Discussion, and the inter-peak period (IPP) of the associated results.

## 6.1 Waves or convecting density structures?

Our analysis does indeed deduce the *wavelength* of the ripples, but we cannot say with confidence whether these are truly waves (driven by gradient drift instabilities, with a wavelength and a frequency), or convecting density structures originating in the cusp (driven either by ExB drift or a pulsating flux transfer event mechanism, with an inter-structure spatial distance and a periodicity). Nevertheless, the results herein, together with our previous studies (Hargreaves and Birch, 2018; B&H), suggest that the ripples are persistent and widespread in the F-region, and are not a transient phenomenon.

Evidence that density structures with very similar dynamics exist at lower layers of the ionosphere in the form of absorption patches (not waves) can be found in a dual instrument study of the D and E regions by Birch et al. (2013) involving the EISCAT VHF radar at Tromsø and the IRIS imaging riometer at Kilpisjärvi. A sequential series of absorption patches was detected by the riometer between altitudes 70 and 120 km in the morning sector (0230-0615 UT) with median dynamics similar to the results herein: a periodic separation of 19 minutes (343 km), and a westerly speed of 23.1 km/min (385 m/s). Furthermore, recent tests on the VHF data from this study reveal the existence of distinct ripples in the electron content with a periodicity of 20 minutes, in close agreement with the results from the absorption patches.

[It was suggested in Birch and Hargreaves (2020a, 2020b) that the source of the ripples at L1 might lie in p- and g-mode solar oscillations, or Alfvén waves in the solar corona. For further details the reader should consult these references, and citations therein.]

## 7 Summary

- From observations with the 42m ESR radar over a total of 10.6 hours, the median inter-peak period of the ripples in F-region electron content was 20 minutes, with quartiles

at 17 and 28 minutes.

- From the same observations, the median inter-peak period of the ripples in electron density at height 300 km was 19 minutes, with quartiles 14 and 25 minutes.
- During the two selected intervals in the noon sector, the average plasma flow speed was 462 m/s (height range 213 to 389 km) and 450 m/s (height 300 km), and the direction was approximately W.
- During the selected interval in the night sector, the plasma flow speed was 280 m/s (height range 213 to 389 km) and 270 m/s (height 300 km), and the direction was approximately S.
- From these flow speeds, and the average inter-peak period, the wavelength of the ripples was estimated:
  1. in the noon sector, 581 km (height range 213 to 389 km) and 470 km (at 300 km)
  2. in the night sector, 454 km (height range 213 to 389 km) and 421 km (at 300 km).
- On average, the wavelength is greater in the noon sector than in the night sector by 127 km (height range 213 to 389 km) and 49 km (at 300 km).
- The direction of flow of the plasma in which the ripples are embedded was shown to agree in general terms with the circulation patterns deduced from modelled data based on SuperDARN observations.
- Fluctuations with similar frequencies have been reported over a broad range of local times and magnetic latitudes (L-values from 1.3 to 20.4), including some with similar flow speeds, directions and wavelengths in the D and E regions.
- The analysis of the 32m circular scan (either with respect to the field, as in this case, or in a vertical configuration) provides a method of determining the actual flow speed and direction from the line-of-sight velocity along the beam (given steady-state conditions).
- Though our analysis provides the *wavelength* of the ripples, we cannot say with any certainty whether these are waves or convecting density structures originating in the

cusps, so this term should be treated with caution.

## Acknowledgements

The authors would like to express their gratitude to the EISCAT staff for their assistance. In particular, we thank I. McCrea and A. Kavanagh for setting-up the experiment, I. Haggström for co-ordinating it, and the scientists and engineers at Svalbard for running it. We also thank the SuperDARN team for provision of the F-region circulation maps.

## References

- Birch, M.J., Hargreaves, J.K., Bromage, B.J.I, Properties of auroral radio absorption patches observed in the morning sector using imaging riometer and incoherent-scatter radar. *Journal of Atmospheric and Solar-Terrestrial Physics*. 105-106, 262-272, 2013.
- Birch, M.J., Hargreaves, J.K., Quasi-periodic ripples in high latitude electron content, the geomagnetic field, and the solar wind. *Nature (Scientific Reports)*, 10:1313 <https://doi.org/10.1038/s41598-019-57201-4>, 2020a.
- Birch, M.J., Hargreaves, J.K., Quasi-periodic ripples in the heliosphere from 1 to 40 AU. *Adv.Sp.Res.* <https://doi.org/10.1016/j.asr.2020.08.030>, 2020b.
- Greenwald R.A., Baker K.B., Dudeney J.R., Pinnock M., Jones T.B., Thomas E.C., Villain J.-P., Cerisier J.-C., Senior C., Hanuise C., Hunsucker R.D., Sofko G., Koehler J., Nielsen E., Pellinen R., Walker A.D.M., Sato N., Yamagishi H., DARN/SuperDARN: A global view of the dynamics of high-latitude convection, *Space Science Reviews* vol. 71, pp.761796, 1995.
- Guo, J., Wei, F., Feng, X., Liu, H., Wan, W., Yang, Z., Xu, J., Liu, C., Alfvén waves as a solar-interplanetary driver of the thermospheric disturbances. *Sci. Rep.* 6, 18895; doi: 10.1038/srep18895, 2016.

- Guo, J., Wang, Z., Zheng, J., Cui, J., Wei, Y., Wan, W. Unusual multiple excitation of large-scale gravity waves by successive stream interactions: The role of Alfvénic fluctuations. *J. Geophys. Res., Space Physics*, 124, 62816287. <https://doi.org/10.1029/2019JA026655>, 2019
- Hargreaves, J.K., Birch, M.J., Observations by incoherent scatter radar of related D- and F-region structuring at very high latitude, *Journal of Atmospheric and Solar-Terrestrial Physics*, 174, 5-16, 2018.
- Hayes L.A., Gallagher P.T., McCauley J., Dennis B.R., Ireland J., Inglis A., Pulsations in the Earths Lower Ionosphere Synchronized With Solar Flare Emission, *Jnl. Geophys. Res.*, 122, 98419847. <https://doi.org/10.1002/2017JA024647>, 2017.
- Livneh D.J., Seker I., Djuth F.T., Mathews J.D., Omnipresent vertically coherent fluctuations in the ionosphere with a possible worldwide-midlatitude extent, *Jnl. Geophys. Res.*, vol. 114, A06303, doi:10.1029/2008JA013999, 2009.
- Lockwood M., Cowley S.W.H., Freeman, M.P., The excitation of plasma convection in the high-latitude ionosphere, *Journal of Geophysical Research*, Volume 95, Issue A6, p. 7961-7972, 1990.
- Prikryl P., Muldrew D.B., Sofko G.J., Ruohoniemi J.M., Solar wind Alfvén waves: a source of pulsed ionospheric convection and atmospheric gravity waves, *Annales Geophysicae*, 23: 401417, 2005.
- Villante, U., Francia P., Vellante M., Long period magnetospheric oscillations at discrete frequencies: the results of a multi-station analysis, *Advances in Space Research* 46, 460467, 2010.
- Zhang, S.R., Holt, J.M., McCready, M., High latitude convection based on long-term incoherent scatter radar observations in North America, *Journal of Atmospheric and Solar-Terrestrial Physics*, 69, 12731291, 2007.

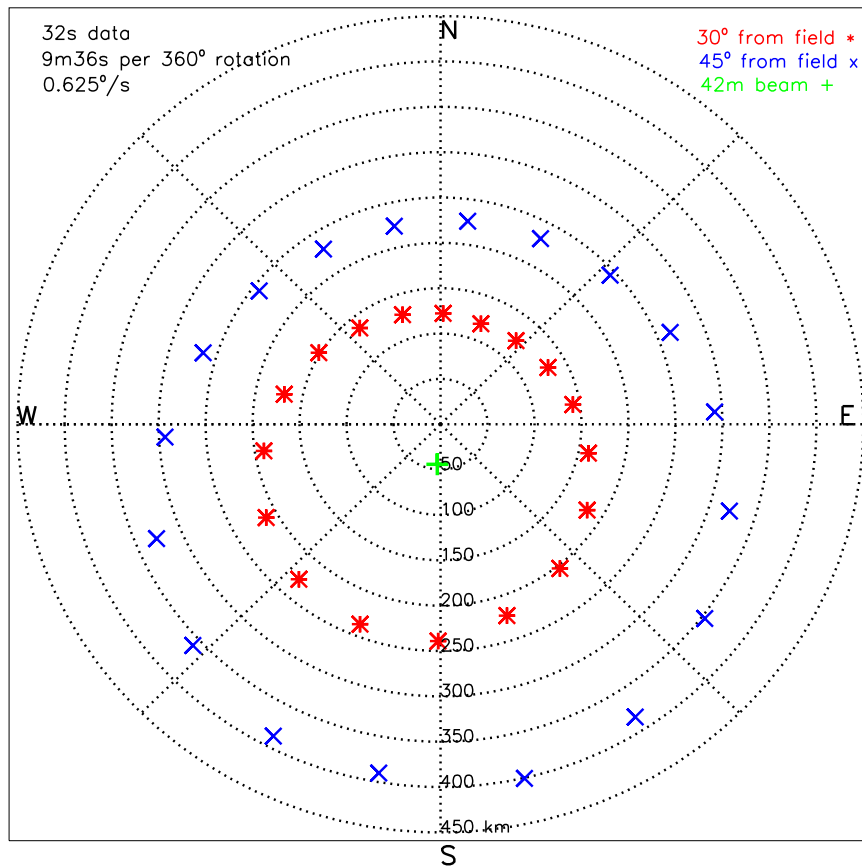


Figure 1: Scan pattern - distance from 32m antennae (km) at height 300 km. (Green: position of 42m field-aligned beam; red: data-points at  $30^\circ$  from field; blue: data-points at  $45^\circ$  from field.) The patterns are not symmetrical with respect to the 42m beam because the section is horizontal, not orthogonal to that beam.

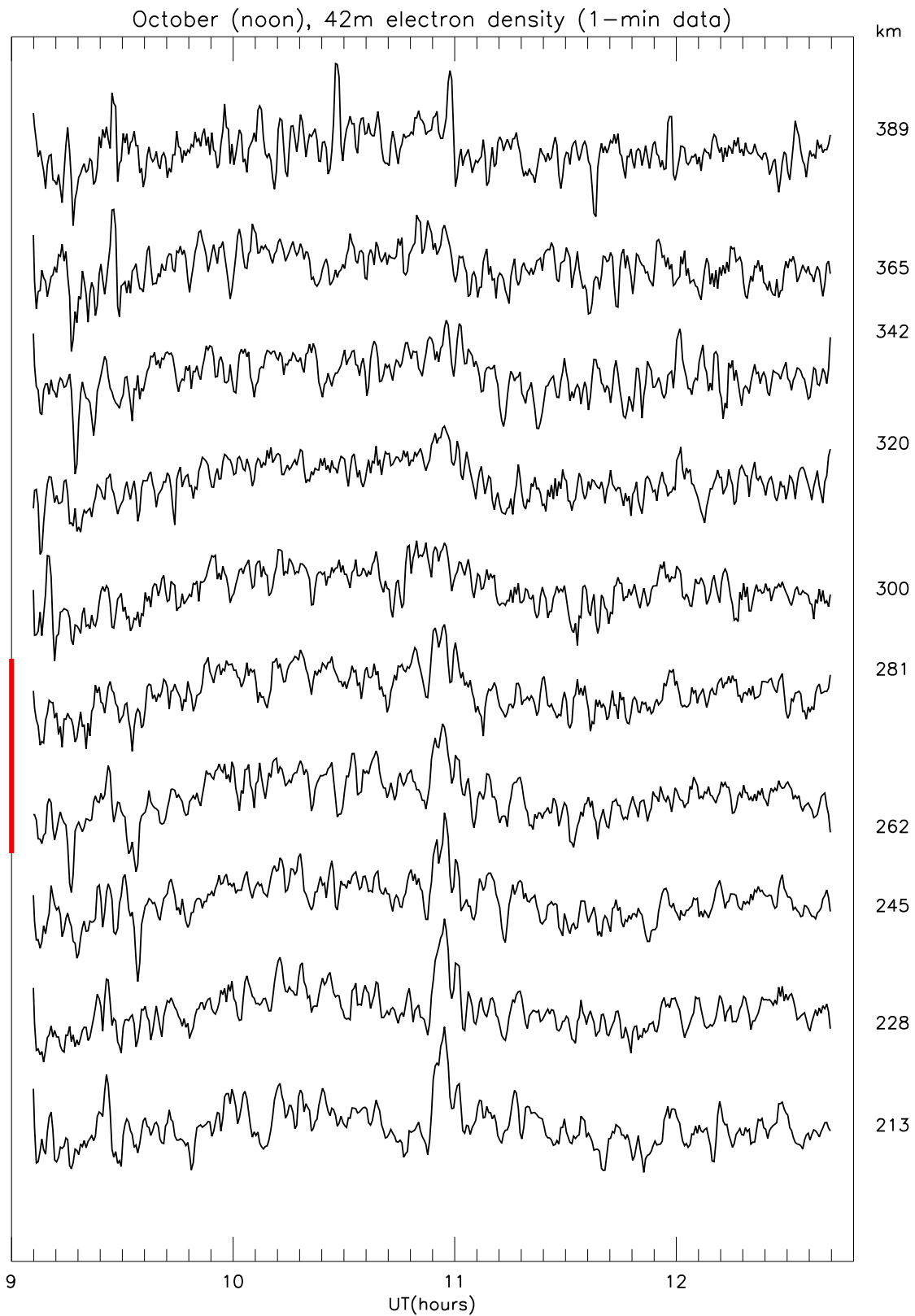


Figure 2: Variations in electron density from the 42m antenna on October 1, for heights from 213 to 389 km, on a log scale. (The vertical red bar shows a factor of 10 variation.)

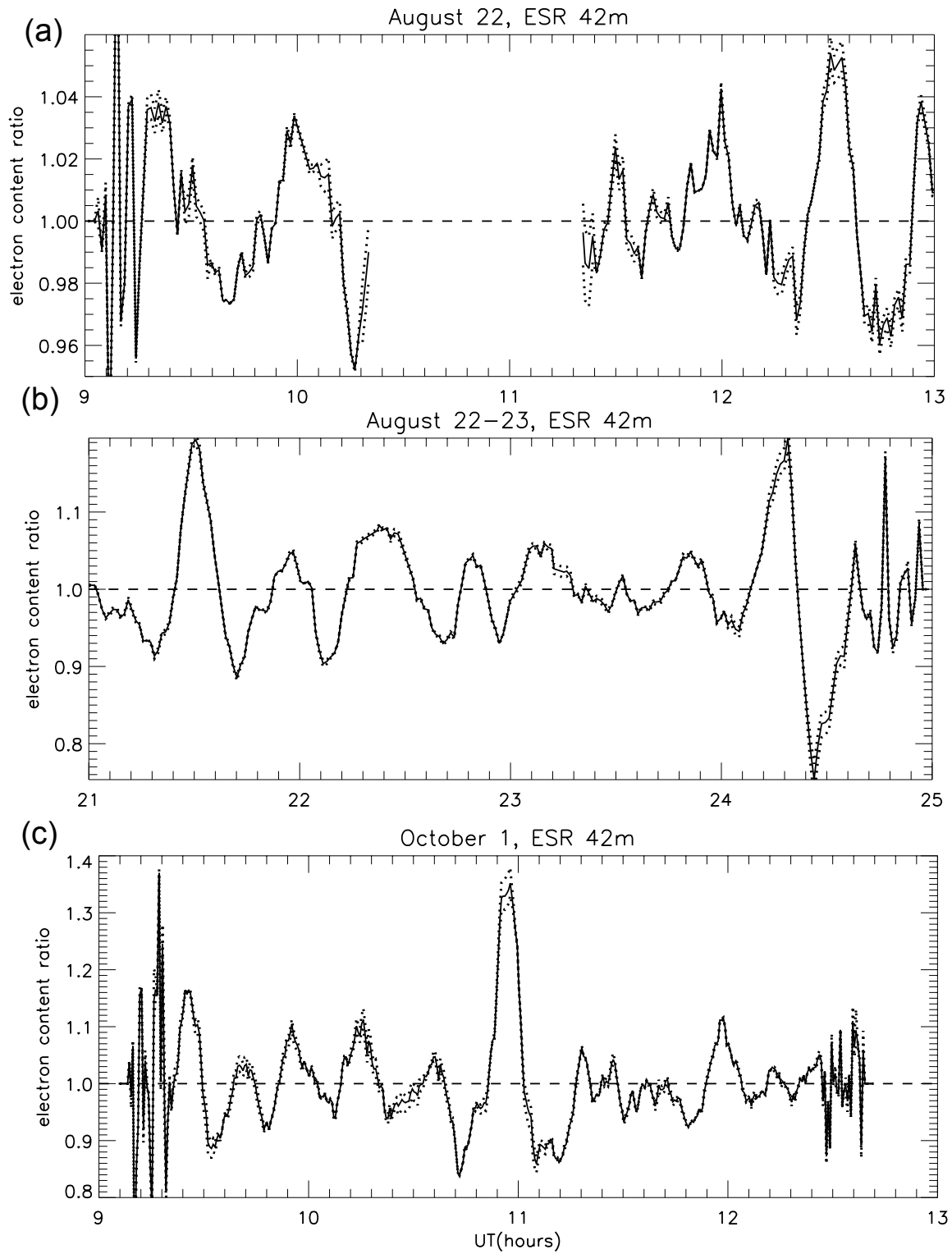


Figure 3: Electron content ratio from the 42m antenna: (a) noon sector on August 22; (b) midnight sector on August 22-23; (c) noon sector on October 1. (The dotted lines denote the  $3\sigma$  errors.)

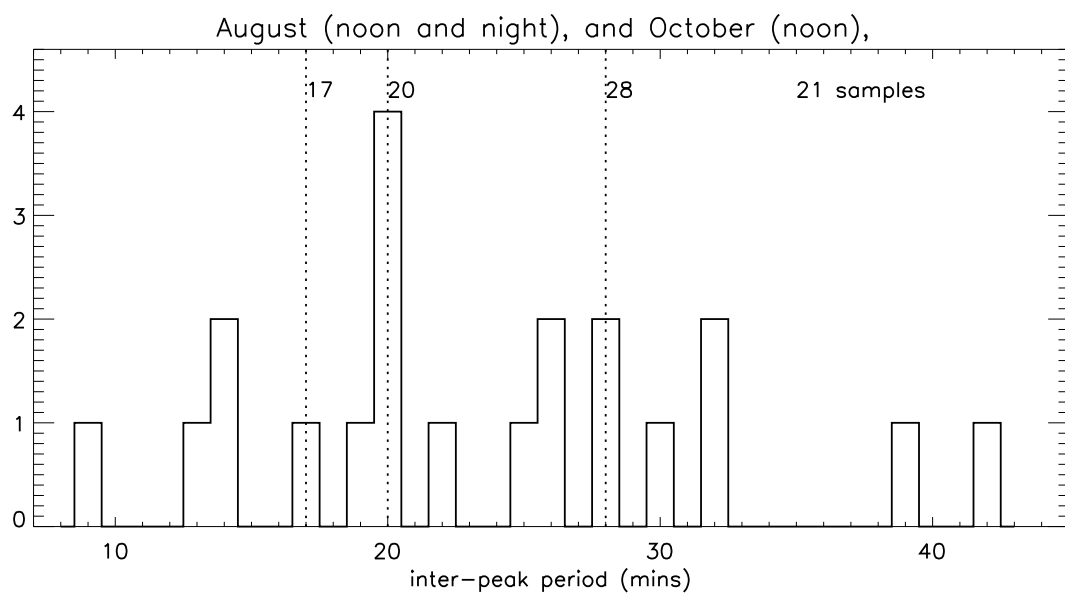


Figure 4: Histogram of 42m electron content ratio inter-peak periods for the 3 observing periods combined, showing median, quartiles, and number of samples.

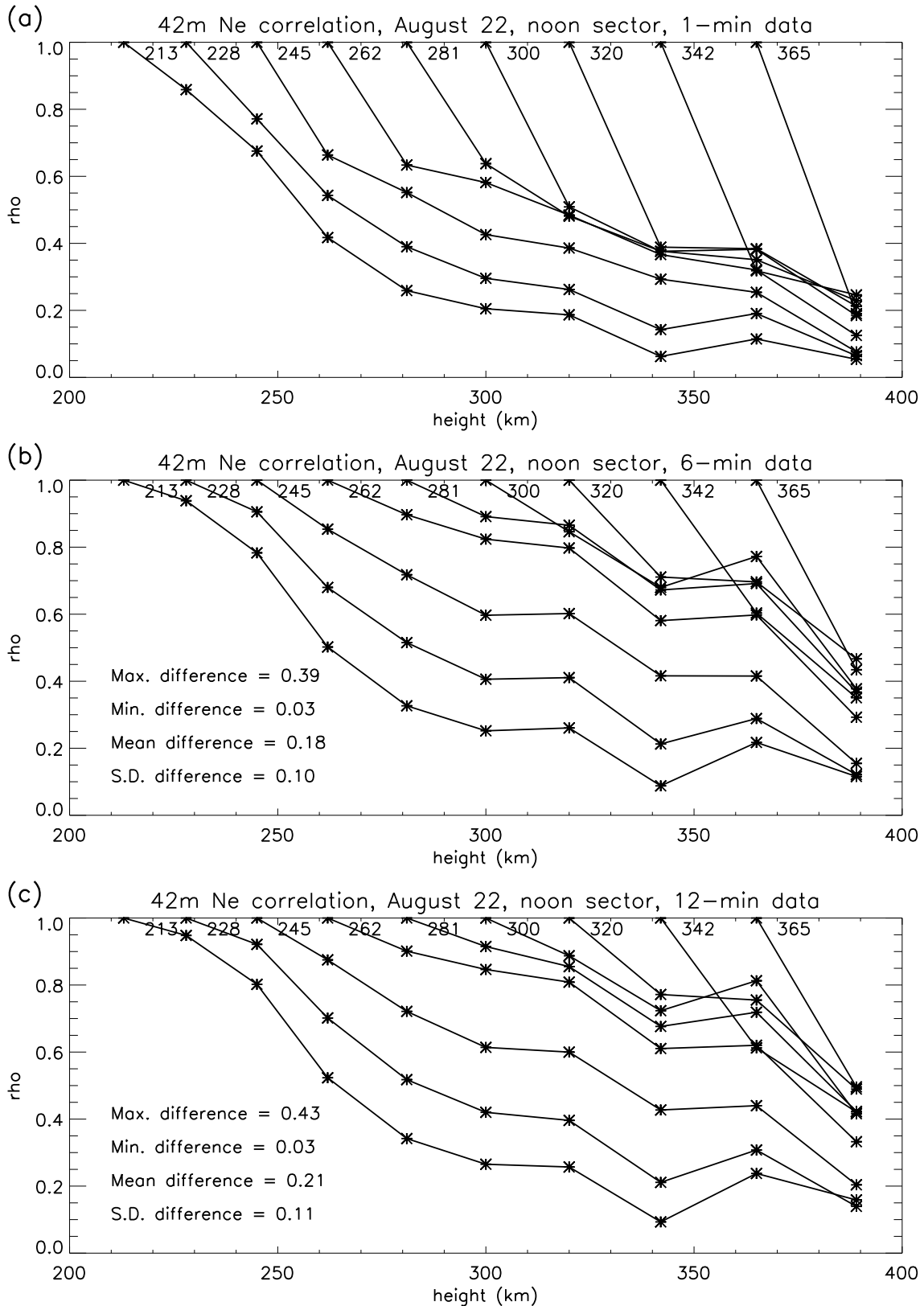


Figure 5: Correlation of the 42m electron density time series for the noon period on August 22 (example), for all pairs of heights: (a) 1-minute time series; (b) 6-minute smoothing; (c) 12-minute smoothing. (SD = standard deviation.)

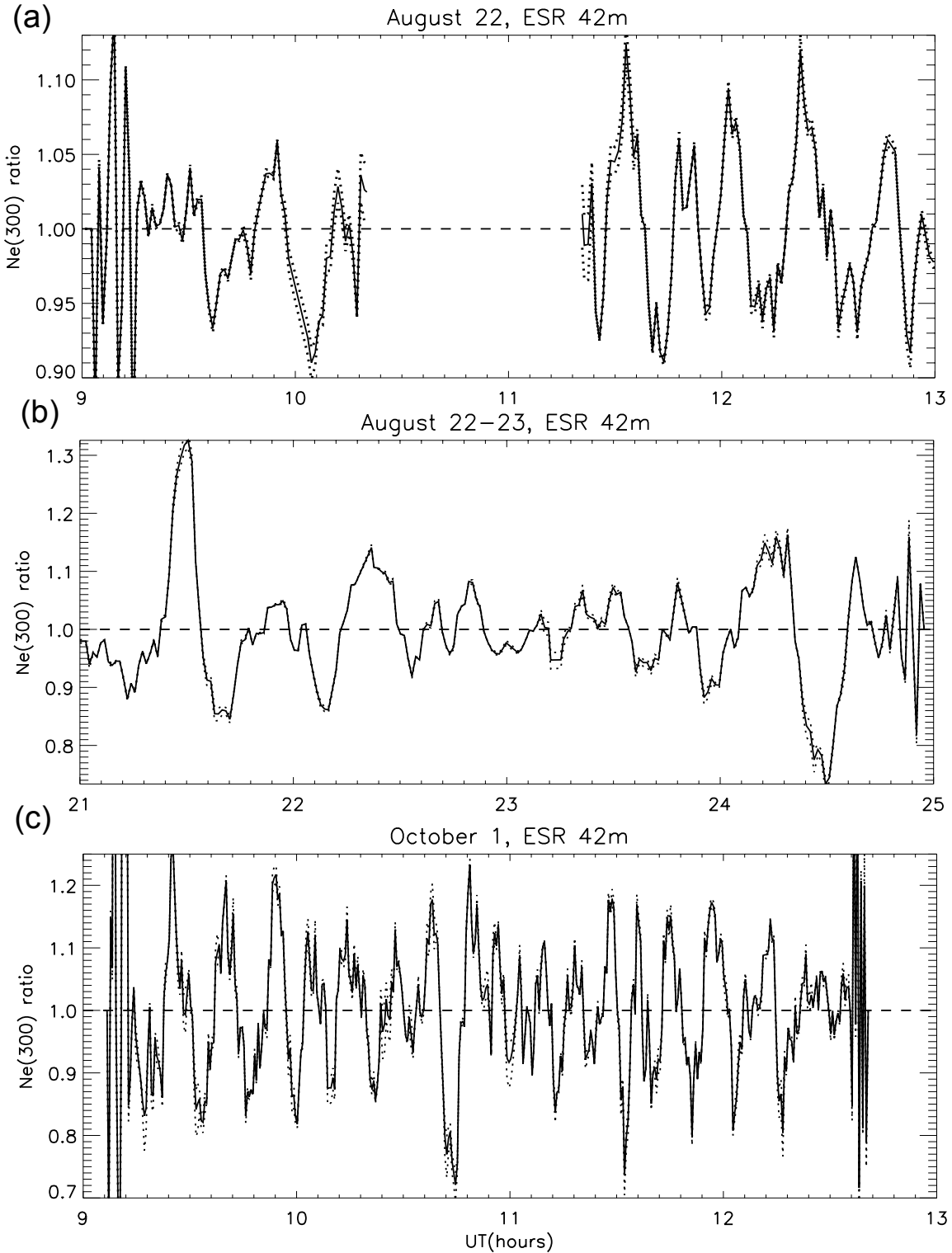


Figure 6: Electron density ratios from the 42m antenna at height 300 km: (a) noon sector on August 22; (b) midnight sector on August 22-23; (c) noon sector on October 1. (The dotted lines denote the  $3\sigma$  errors.)

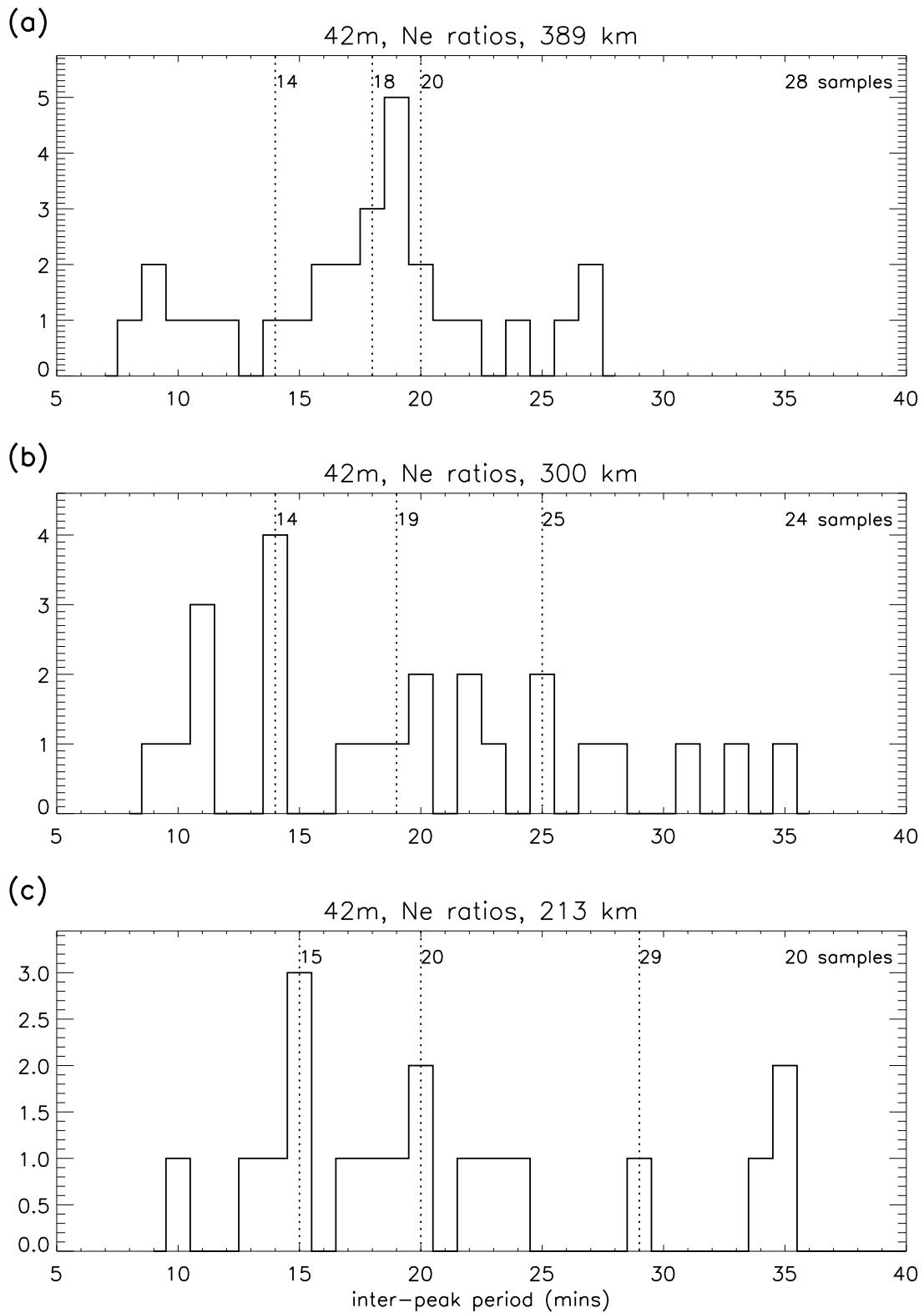


Figure 7: Histograms of 42m Ne ratio IPPs for the 3 observing periods combined, at 3 selected heights: (a) 213 km; (b) 300 km; (c) 389 km.

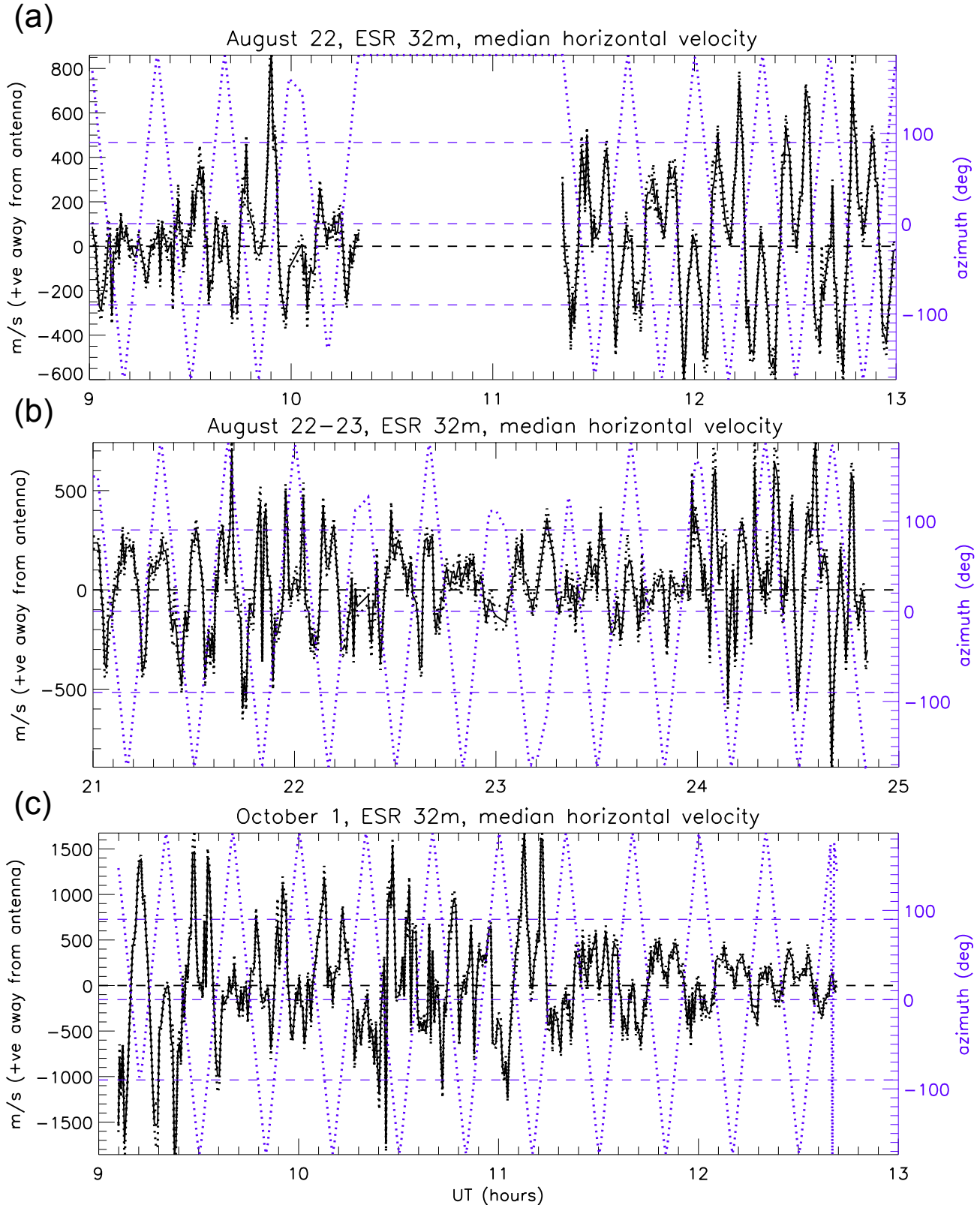


Figure 8: Median horizontal 32m velocity for the 3 observing periods (32s data): (a) noon sector on August 22; (b) midnight sector on August 22-23; (c) noon sector on October 1. (The dotted blue lines denote the antenna azimuth (positive clockwise from N) and the dotted black lines are the  $3\sigma$  errors.)

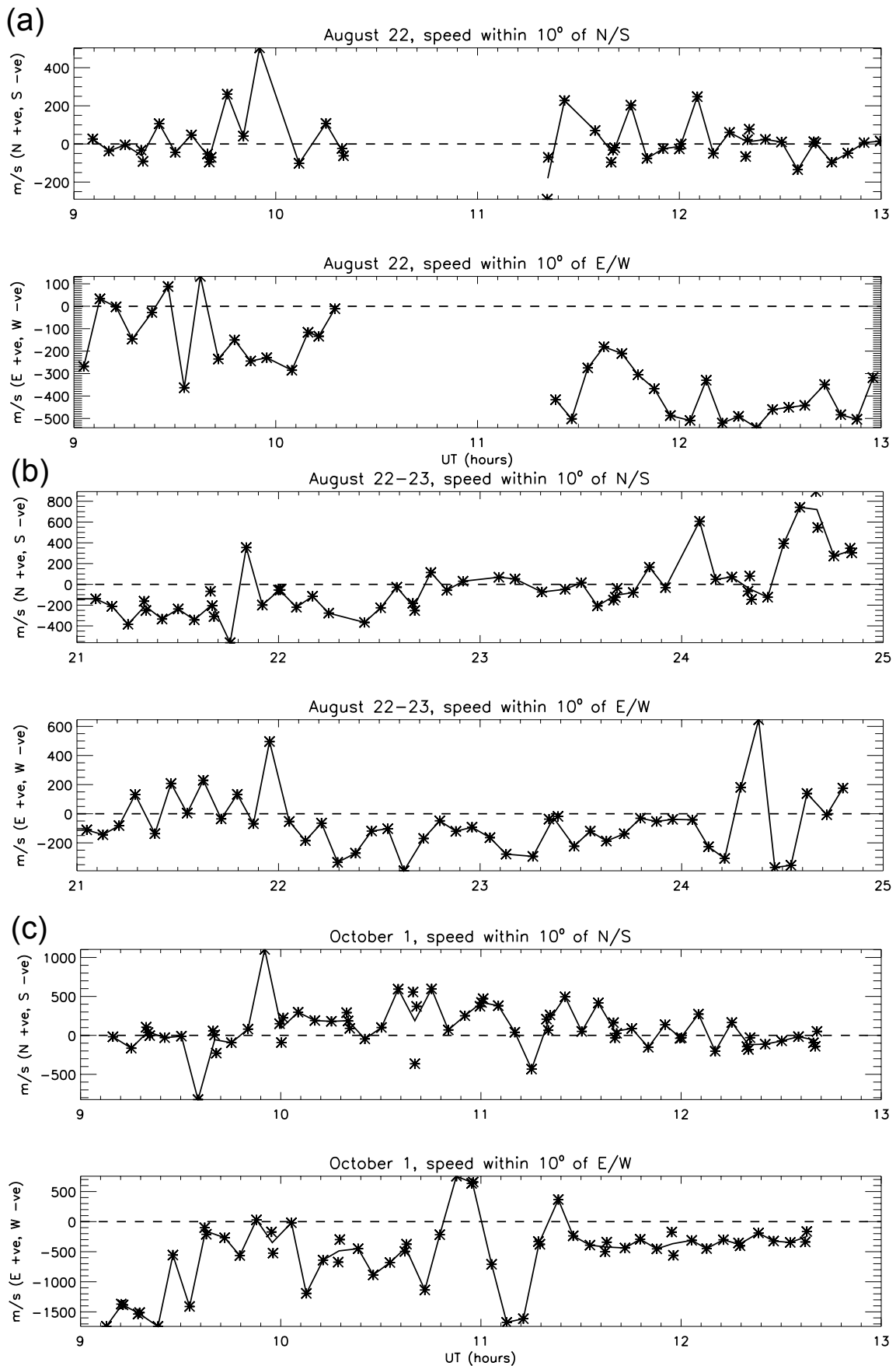


Figure 9: Velocities within 10° of N/S, and E/W (32s data): (a) noon sector on August 22; (b) midnight sector on August 22-23; (c) noon sector on October 1.

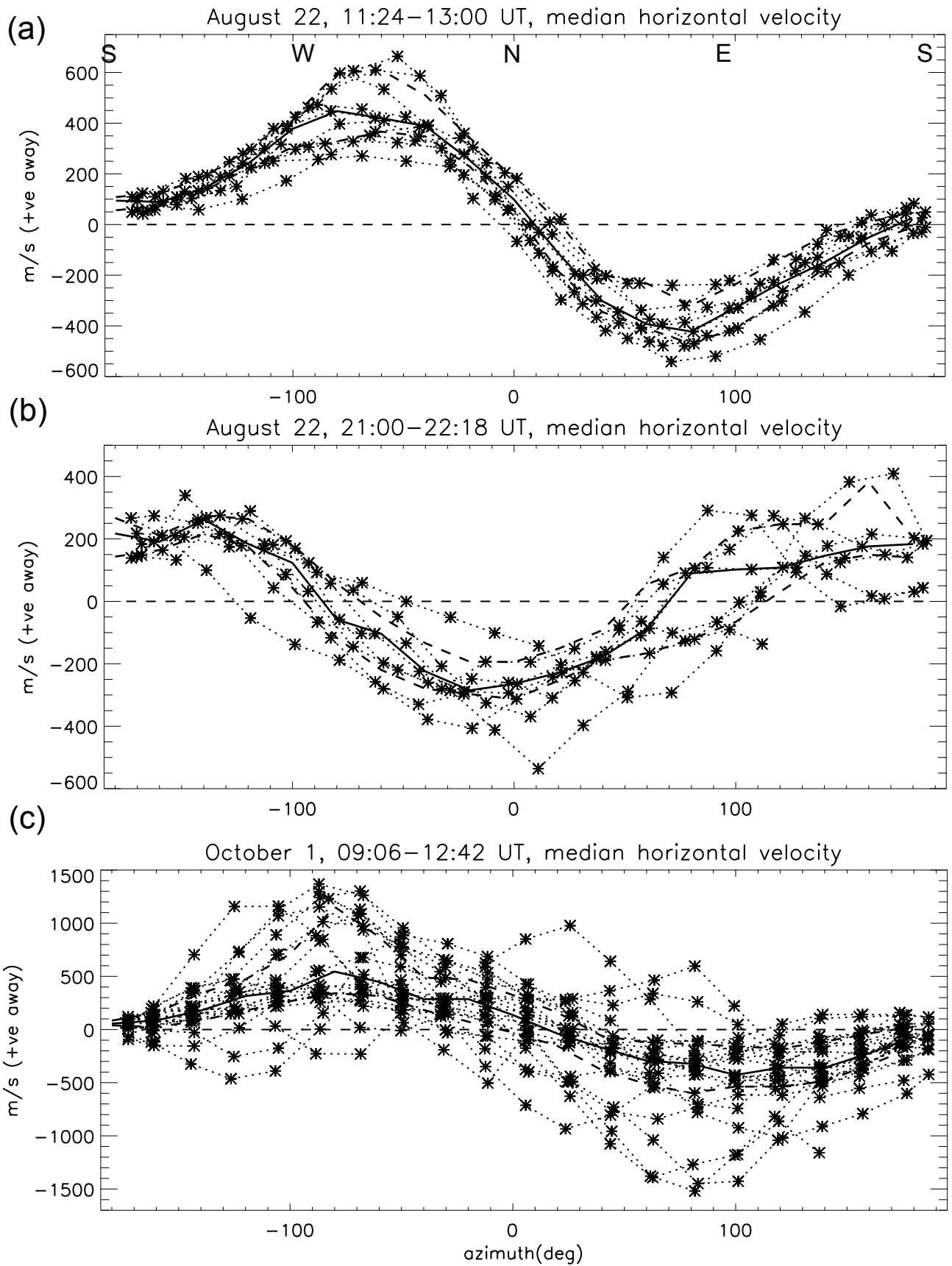


Figure 10: Median horizontal 32m velocity against azimuth for the 3 selected intervals (smoothed to 64s): (a) August 22, 11:24-13:00 UT; (b) August 22, 21:00-22:18 UT; (c) noon sector on October 1. (The solid lines represent the medians of the datapoints in  $20^\circ$  intervals for the  $30^\circ$  and  $45^\circ$  sweeps combined, and the dashed lines are the quartiles. The dotted lines connect each  $360^\circ$  rotation of the antenna.)

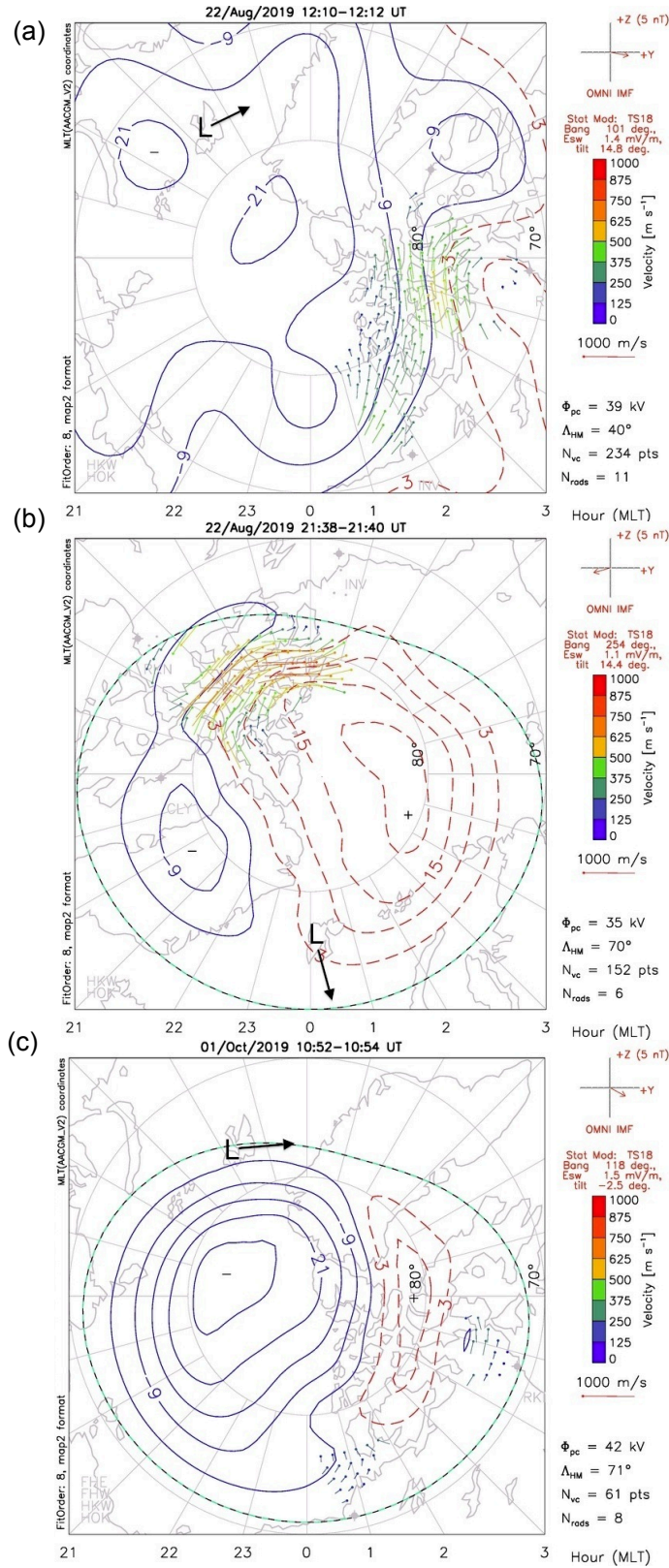


Figure 11: F-region circulation maps from the SuperDARN coherent radar network, near the middle of each selected interval in 2019: (a) August 22 (12:10-12:12 UT); (b) August 22 (21:38-21:40 UT); October 1 (10:52-10:54 UT). (L marks the location of the ESR antennae at Longyearbyen, and the arrows indicate the approximate flow directions in Table 4.)